PAPER

Check for updates

A La³⁺-doped TiO₂ nanoparticle decorated functionalized-MWCNT catalyst: novel electrochemical non-enzymatic sensing of paraoxon-ethyl†

Raja Nehru [ID] and Shen-Ming Chen [ID] *

The development of novel chemical sensors for pesticide detection has found particular application in the area of environmental monitoring. However, designing primary sensors as weapons to destroy contaminants (*e.g.*, paraoxon-ethyl) in water and soil remains a challenge. Herein, we show different strategies, such as modification of TiO₂ NPs through La³⁺ doping and decoration of f-MWCNTs, which can provide possibilities for notable developments in electrocatalytic performance. Using this approach, we introduce an active La³⁺ doped TiO₂ NP decorated f-MWCNT electrocatalyst for pollutant monitoring applications. Thereby, our findings move towards an outstanding LOD (0.0019 μM) performance, high selectivity, and exceptional sensitivity (7.6690 μA μM⁻¹ cm⁻²) on an as-presented catalytic platform for a PE sensor. Interestingly, the practical applicability of the suggested catalyst shows a rich sensing platform for PE-contaminated environmental samples.

1. Introduction

Organophosphate pesticides (OPs) are considered to be a premier type of pesticide owing to their extraordinary accomplishments in pest control but have caused prodigious pollution in the environment, and in food and water. Paraoxon-ethyl (PE) is an organophosphate pesticide, and is broadly used to control pests/insects and increase the yields of a large number of agricultural crops.[1] OP pesticides are mainly employed for the cultivation of fruits, wheat, rice, garlic, beans, and cotton *via* a spraying technique.[2] The long-term persistence of pesticides and insecticides are complexities in the ecological system; usage of a large quantity of PE causes a significant issue in groundwater contamination. However, PE can easily penetrate pure groundwater and can migrate through the food chain in day-to-day consumption. Meanwhile the level of intake of PE-contaminated foods is increasing, which in turn causes severe health risks, including diarrhea, vomiting, poor vision, headaches, and critical neurotoxic effects.[3–5] Therefore, the U.S Environment Protection Agency (EPA) stated that PE is an extremely toxic substance for both animals and human beings.[6]

Environmentally friendly and efficient technologies for the detection of pesticides are highly desired. Nowadays, there are many possible conventional techniques for the detection of

pesticides in contaminated water, such as high-performance liquid chromatography (HPLC) and HPLC-MS/MS,[7–9] gas chromatography and ultra-violet spectrophotometry,[10,11] and high-performance capillary zone electrophoresis.[12] Among these methods, those based on electrochemical sensors have been extensively used and have shown satisfactory results for OP analysis due to their uncomplicated operation, fast response, on-site detection, low-cost impact, extraordinary sensitivity, and selectivity.[6]

Over past decades, various metal oxides have been investigated to enhance the electrochemical catalytic activity towards features needed for pesticide monitoring in the field of electrochemistry.[13] To date, there has been interest in exploring the chemical and bio-sensing of several semiconducting metal oxides due to their tunable redox and conducting characteristics, affordability, high level of sensitivity, fast response time, and ability to classify the species of analytes. Many n-type and p-type semiconducting metal oxides have been studied, including ZnO, SnO₂, TiO₂, Fe₃O₄, NiO, and many others. Among the others, titania (TiO₂) has been used to construct a variety of novel materials in the fields of electrochemical sensors,[14] and catalytic reduction.[15–20] TiO₂ is a typical semiconductor and a versatile catalyst, which shows high stability, low cost, and non-toxicity for practical applications. Because of these considerations, TiO₂ NPs are a prominent key factor for studying catalytic behavior towards pollutant monitoring, while TiO₂ NPs are of great interest for their industrial importance. However, systematic efforts are still needed to develop a superior electrocatalyst towards the electrochemical sensing of

Department of Chemical Engineering and Biotechnology, National Taipei University of Technology, Taipei 10608, Taiwan. E-mail: smchen1957@gmail.com; nrajache@ gmail.com

† Electronic supplementary information (ESI) available. See DOI: 10.1039/d0na00260g

pollutants due to the electron–hole pair recombination of TiO_2 NPs. To overcome these issues, the doping phenomenon is a powerful strategy to improve the catalytic performance of TiO_2 NPs in an electrochemical sensor platform, which can be accomplished by different approaches, such as doping with non-metals, transition metals, or rare-earth metals.[21–23] Herein, the utilization of rare-earth elements is a significant idea to enhance catalytic activity towards pesticide detection; the rare-earth dopants act as an electron sink on the surface of the semiconductors, which reduces electron–hole pair recombination.[24] Notably, when doping La^{3+} into TiO_2 NPs, an increase in the concentration of oxygen vacancies in the unit cell of the doped TiO_2 structure is expected. This feature promotes the migration of oxygen ions through the lattice oxide and provides the material with high oxygen ion conductivity. Besides, it is expected that the La^{3+} doped TiO_2 NPs will increase chemical adsorption on the semiconductor surfaces, which will help to enhance the sensing performance in pollutant determination using chemical sensors. Carbon materials have noteworthy high electrical conductivity, good mechanical strength, a high specific surface area, and catalytic properties. Among carbon nanotubes (CNTs) both single-walled and multi-walled carbon nanotubes (MWCNTs) have become attractive electrode materials in recent decades for the detection of pesticide pollutants. The f-MWCNTs with La^{3+} doped TiO_2 NPs will be excellent candidates for use as substrates, and might have a notable impact on the electrochemical sensing platform due to their synergetic effect.[25]

In this study, we propose the decoration of f-MWCNTs with La^{3+} doped TiO_2 nanoparticles (NPs) by an ultrasound sonication process. Using this composite, we analyzed the electrocatalytic sensing behavior for organophosphate pesticide (PE), according to the electrochemical schematic illustration shown in Scheme 1. The results showed that we had achieved remarkable sensing behavior towards the detection of PE with excellent selectivity and selectivity. Furthermore, the functions

of the modified electrode materials show long-term stability and real-time applicability, which will help to accomplish the challenge of finding a catalyst for the detection of PE-contaminated groundwater samples.

2. Experimental

2.1. Chemicals and reagents

Pure-MWCNTs, titanium(IV) isopropoxide (97%), lanthanum nitrate hexahydrate, $La(NO_3)_3 \cdot 6H_2O$ (99.999%), isopropyl alcohol (IPA), and paraoxon-ethyl ($O_2NC_6H_4OP(O)(OC_2H_5)_2$) (analytical standard) were purchased from Sigma-Aldrich; all the reagents were employed without additional purification. The phosphate buffer (PB) (0.05 M) electrolyte was prepared using Na_2HPO_4 (dibasic, anhydrous), and NaH_2PO_4 (monobasic, anhydrous). All the electrolytes were prepared in deionized (DI) water to carry out the electrochemical investigations.

2.2 Synthesis of functionalized multiwall carbon nanotubes (f-MWCNTs)

The MWCNTs were functionalized according to a previously reported procedure.[26] Typically, the pristine-MWCNTs (1 g) were dispersed into 50 mL of a 1 : 1 (v/v) ratio of HNO_3 (67%) and H_2SO_4 (97%) and kept at 60 °C for 30 min under constant magnetic stirring. Afterwards, the well-dispersed solution was ultra-sonicated for 6 h (37 kHz), and then it was kept at room temperature. Subsequently, the f-MWCNT residue was washed with DI water to remove acid by centrifugation. The black residue of f-MWCNTs was allowed to dry at room temperature.

2.3 Synthesis of La^{3+} doped TiO_2 NPs

The mixed-phase TiO_2 (anatase/rutile) with La^{3+} doped NPs was synthesized via the sol–gel method by polycondensation and hydrolysis of titanium tetra-isopropoxide (TTIP) and
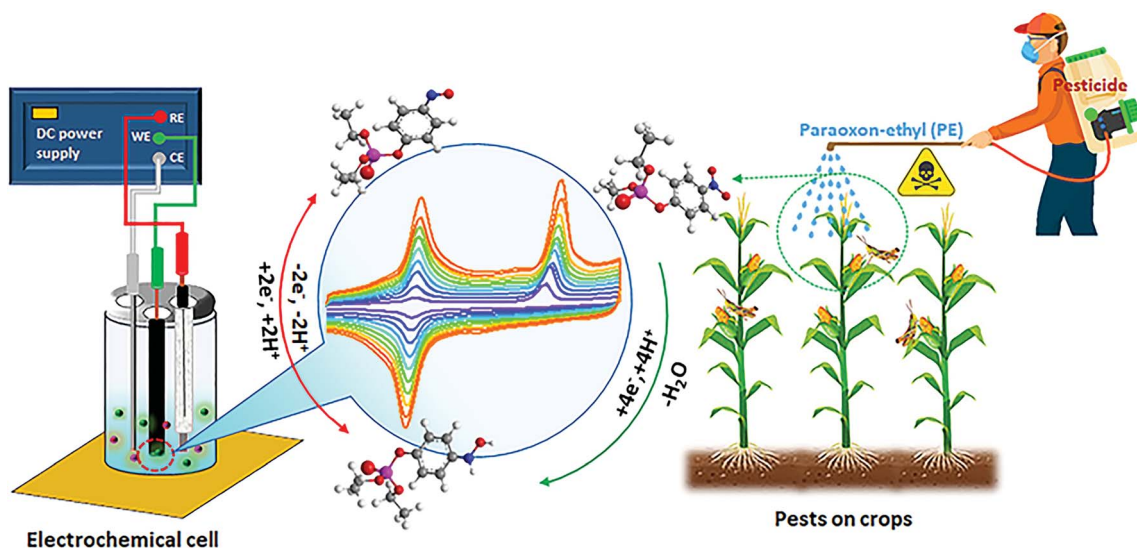
Scheme 1 Schematic illustration for the development of novel chemical sensors for pesticide detection.

a lanthanum precursor (lanthanum nitrate hexahydrate (99.999% purity)) in the presence of isopropanol. Typically, TTIP (13 mL) was dissolved in 65 mL of isopropanol in a beaker and then the solutions were mixed well and continuously until a homogeneous solution of the suspension was obtained. Subsequently, a separate mixture of a 1 : 1 (v/v) ratio of isopropyl alcohol (45 mL) and water (45 mL) was added into the homogenous suspension drop-by-drop and mixed completely for up to 30 min. Then the lanthanum precursor (10%) was slowly added into the reaction mixture solution with continuous stirring. Afterward, 1 mL of concentrated (68%) nitric acid was added dropwise into the reaction compounds followed by vigorous stirring for thorough dispersion. Subsequently, the reaction compounds were kept under continuous stirring (2 h), which was followed by aging at room temperature for 24 h. The reaction mixture of La^{3+} doped TiO_2 NPs was centrifuged and drenched with isopropanol and water and then washed many times and dried at 343 K for 12 h. Finally, the obtained La^{3+} doped TiO_2 NPs underwent an annealing process which was carried out with a 2 °C min^{-1} ramp rate at 773 K under an air atmosphere. The TiO_2 nanomaterial was prepared by an identical procedure with a tiny modification (without the presence of a dopant). An illustration of the synthesis procedure for La^{3+} doped TiO_2 NPs is shown in Scheme 2.

2.4 Synthesis of La^{3+} doped TiO_2 NP decorated f-MWCNTs

The La^{3+} doped TiO_2 NP decorated f-MWCNTs were sono-chemically synthesized with three different ratios of f-MWCNTs and TiO_2 (1 : 1, 2 : 1, and 3 : 1). In a typical composition, the f-MWCNTs were dispersed in 100 mL of DI water and then ultrasonicated for 30 min. Then as-prepared La^{3+} doped TiO_2 was added to the suspension of f-MWCNT solution. The attained solution mixture was ultra-sonicated for 1 h (at 37 kHz). After completing the sonication process, the suspension settled down at room temperature. Subsequently, the collected product was centrifuged with DI water and ethanol several times. The final residue was dried at room temperature, and then it was designated as La^{3+}-doped TiO_2 NP decorated f-MWCNTs.

2.5 Characterization

Powder X-ray diffraction (XRD) was performed using a Bruker D8 Advance X-ray diffractometer. Fourier transform infrared spectroscopy (FTIR) used a CHI 10000 C FT/IR-6600 instrument. Transmission electron microscopy (TEM) and energy-dispersive X-ray spectroscopy (EDS) elemental analysis were recorded using a TEM-JEM-2100F (HR) instrument. XPS measurements were analyzed with a Kratos Axis Ultra spectrometer, using focused monochromatized Al Kα radiation ($h\nu$) of 1486.6 eV. The specific surface area and the pore size
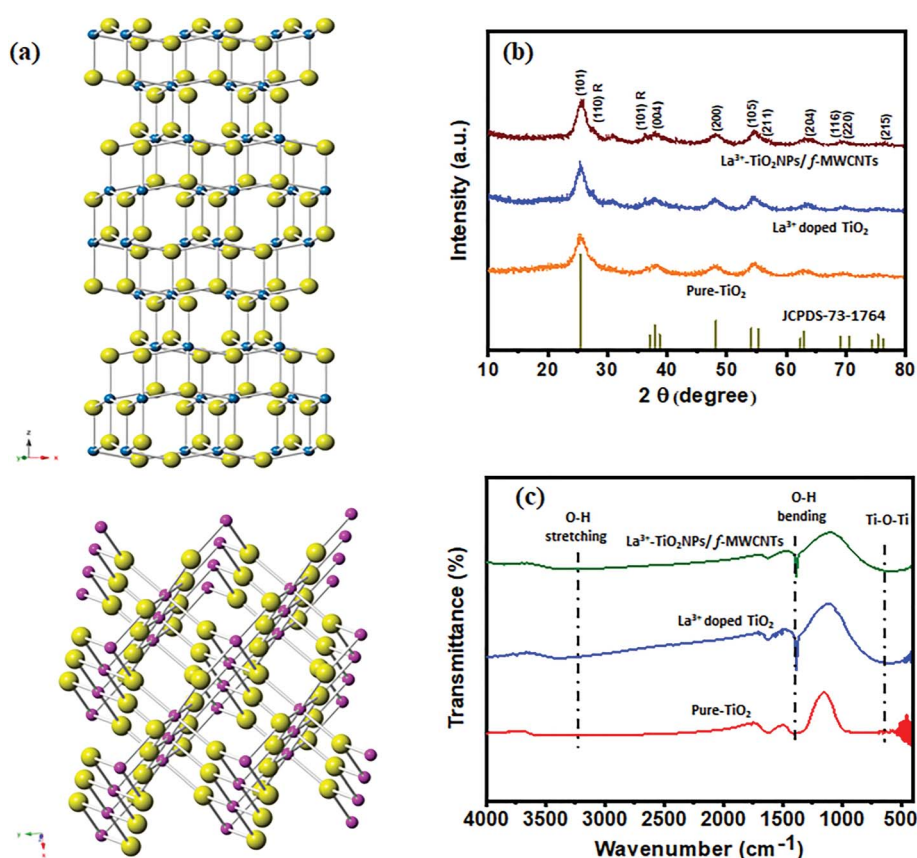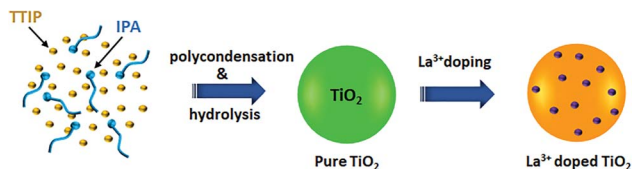

Fig. 1 (a) The crystal structure of TiO_2 (anatase and rutile), (b) X-ray powder diffraction patterns, and (c) FTIR spectra of pure-TiO_2, La^{3+} doped TiO_2, La^{3+} doped TiO_2 NP decorated f-MWCNTs.

Scheme 2 Schematic illustration of the synthesis procedure for La^{3+} doped TiO$_2$ NPs.

distribution were analyzed by using the Brunauer–Emmett–Teller (BET) and Barrett–Joyner–Halenda (BJH) methods. The electrochemical characterizations and analytical techniques were implemented by two different voltammetry techniques (CV & DPV) using CHI instruments (1205 C and CHI 900, USA).

2.6. Fabrication of La^{3+} doped TiO$_2$ NP decorated f-MWCNT modified electrode

The La^{3+} doped TiO$_2$ NP decorated f-MWCNTs were fabricated onto the GCE surface *via* the drop-casting method. Before the GCE surface modification, the GCE was well-polished with alumina slurry and then washed with DI water to remove the alumina slurry. Typically, 1 mg of La^{3+} doped TiO$_2$ NP decorated f-MWCNT catalyst was dispersed in 1.0 mL of DI water and then ultra-sonicated for 15 min to obtain a uniform mixture. Subsequently, the obtained catalyst (optimized concentration 6 μL) was drop cast on the well-polished GCE surfaces and then allowed to dry at room temperature. The GCE modified with La^{3+} doped TiO$_2$ NP decorated f-MWCNTs was employed for further electrochemical measurements.

3. Results and discussions

3.1 Physicochemical characterizations

First, the La^{3+} doped TiO$_2$ on f-MWCNTs were synthesized *via* the sonochemical method, and the detailed synthesis can found in the Experimental section. The structure and purity of TiO$_2$ NPs were analyzed before doping without La^{3+} ions using powder X-ray diffraction (PXRD).

The observed PXRD pattern was correctly correlated with a tetragonal crystal structure with $I4_1/amd$ symmetry. The crystal structure of anatase and rutile are given in Fig. 1(a). From the XRD pattern, the unit cell parameters can be estimated as $a = 3.7842$ Å, $b = 3.7842$ Å, $c = 9.5146$ Å, and $\alpha = \beta = \gamma = 90°$. The characteristic diffraction peaks of the anatase TiO$_2$ phase were found at 25.6°, 37.9°, 48.1°, 54.5°, 56.0°, 63.5°, 68.2°, 69.7°, and 76.5°, corresponding to the Bragg reflections from the (101), (004), (200), (105), (211), (204), (116), (220), and (215) planes, respectively. Moreover, the specific rutile phase TiO$_2$ NP peak responses were located at 27.5°, and 36.3°, corresponding to the phase responses of (110), and (101), as shown by the orange line in Fig. 1(b). Thus, the observed peak responses of the mixed-phase of TiO$_2$ NPs are in good agreement with the authorized research report (JCPDS: 73-1764). Furthermore, we analyzed the PXRD of La^{3+} doped TiO$_2$, as shown in Fig. 1(b) (blue line), which clearly shows that there is no evidence for the separate

phase formation of La$_2$O$_3$. This suggests that La^{3+} ions diffused on the surface of the TiO$_2$ matrix as small clusters.[27] The ionic radius of La^{3+} (1.15 Å) is bigger than the ionic radius of Ti^{4+} (0.68 Å), and La^{3+} ions cannot enter into the lattice of TiO$_2$; however, Ti^{4+} ions may enter into the lattice of La$_2$O$_3$, leading to a change in the electronic field of La^{3+} and an increase in the electron density and a decrease in the binding energy of La^{3+}. So, it can be concluded that the lattice parameters of the TiO$_2$ NPs remain unchanged after doping with La^{3+} ions due to the ionic radius factor and percentage of La^{3+} as a monoatomic layer on the TiO$_2$ surfaces, which are not detected by XRD.[28,29]

Moreover, the substitution of Ti^{4+} ions by La^{3+} ions means that no distortion will take place on the crystal structure of TiO$_2$. The 3D schematic unit cell representation of the undoped TiO$_2$ and La^{3+} doped TiO$_2$ crystal structures can be seen in Scheme 3(a). Scheme 3(b) shows that the substitution of Ti^{4+} ions by La^{3+} ions takes place *via* doping on the Ti position (La$_{Ti}^{3+}$), which generates interstitial Ti^{3+} ions and oxygen vacancies, as shown by eqn (1).

$$La^{3+} + Ti^{4+} + O^{2-} \rightarrow \\ (La_{Ti}^{3+} + Ti^{4+} + O^{2-}) + Ti^{3+} \text{ interstitial} + O_2 \quad (1)$$
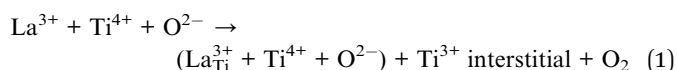
The addition of a rare earth cationic dopant (La^{3+}) in semiconductors of TiO$_2$ crystals modifies their catalytic behavior due to the bandgap energy (Fig. S1(a)–(c)†), which is related to the movement of electrons. The dopant ion creates an intermediate mid-gap state between the valance band and the conduction band, which causes electron hopping. A 2D schematic illustration of the movement of electrons in the TiO$_2$ crystal matrix after doping with La^{3+} can be seen in Scheme 3(c). Furthermore, we analyzed the PXRD of f-MWCNTs and La^{3+} doped TiO$_2$ NP decorated f-MWCNTs. Fig. S1(a)† shows the PXRD of f-MWCNTs, which reveals that the formation of CNTs and high peak intensity vary after the functionalization due to the configuration or extension of a functional group on the boundary edge of the carbon nanotubes.[30] In Fig. S2a,† the peaks located at 25.9° and 42.9° show the characteristic diffraction of (002) and (100) f-MWCNTs, which are in good agreement with an earlier report.[31]

A study of the interplay between f-MWCNTS, TiO$_2$ NPs, La^{3+} doped TiO$_2$ NPs, and La^{3+} doped TiO$_2$ NP decorated f-MWCNTs was carried out using Fourier-transform infrared spectroscopy (FT-IR). The acid-treated oxidized multi-walled carbon nanotubes (Fig. S2b†) show noticeable peaks around 1715 cm^{-1} and 1056 cm^{-1}, contributed by the presence of C=O and C–O stretching vibrations of the carboxylic groups (–COOH).[32] Moreover, the relative intensity of the –OH bands at 3445 and 1635 cm^{-1} shows f-MWCNT associated water molecules and stretching of the carbon nanotube.[33,34] The peak at 2919 cm^{-1} is attributed to the C–H stretching mode of H–C=O in the carbonyl group, which shows the presence of a long-chain alkyl molecule.[35] The peak at 1715 cm^{-1} representing the presence of C=O and C–O stretching vibrations, reveals that the acid treatments introduce carboxylic groups (–COOH) on the surface of the carbon nanotubes. Also, the FTIR spectra of pure TiO$_2$

(red curve), La^{3+} doped TiO$_2$ (blue curve), and La^{3+} doped TiO$_2$ decorated f-MWCNTs (green curve) have been observed in the range between 400 and 4000 cm^{-1}, as shown in Fig. 1(c). This confirms a definite band at 452 cm^{-1}, which has been attributed to Ti–O–Ti that was found in an earlier report.[36] Hence, the metal–oxygen vibration of Ti–O was confirmed, which revealed that the TiO$_2$ nanoparticles were successfully formed in the sol–gel synthesis medium. The absorption bands at 3422 and 1386 cm^{-1} indicate the characteristic vibrations of –O–H stretching and bending vibrations, according to the standard spectra.

In order to investigate the structural features of f-MWCNT$_S$, TiO$_2$ NPs, TiO$_2$ NP decorated f-MWCNT$_S$, La^{3+} doped TiO$_2$ NPs and La^{3+} doped TiO$_2$ NP decorated f-MWCNTs, transmission electron microscopy (TEM) measurements were carried out on all the samples and the results are shown in Fig. 2. A schematic representation of the formation of La^{3+} doped TiO$_2$ NP decorated f-MWCNTs is shown in Fig. 2(a). The TiO$_2$ NPs can be observed in Fig. 2(b), which shows an average particle size of $\approx$50–60 nm. Furthermore, the results for undoped TiO$_2$ NPs obtained by high-resolution transmission electron microscopy (HRTEM) are given in Fig. S3(a).† The corresponding d-spacing of the undoped TiO$_2$ NPs was estimated to be 0.381 nm, in good agreement with the line profile patterns of Fig. S3(c).† Fig. S3(b)† shows the lattice SAED patterns of the TiO$_2$

crystalline (101) plane, in which the observed patterns show a good relationship with the PXRD results for TiO$_2$ NPs. In addition, La^{3+} doped TiO$_2$ NPs were analyzed by TEM measurements at high and low magnification, as shown in Fig. 2(c) and (d). Herein, the La^{3+} doped TiO$_2$ sol–gel mixed (anatase/rutile) phase NPs consist of densely aggregated crystalline nature, which was roughly estimated to be $\approx$ 15 nm. The highly crystalline nature was observed from the SAED pattern of La^{3+} doped TiO$_2$ NPs, as shown in Fig. 2(e). Compared to SAED patterns of pure undoped TiO$_2$ NPs, the La^{3+} doped TiO$_2$ NPs show dislocations due to electric stress, which may due to the La^{3+} ions originating in the TiO$_2$ NPs. From the TEM observation, the particle size of the La^{3+} doped TiO$_2$ NPs has decreased appreciably compared to undoped TiO$_2$ NPs, which reveals that the rare earth element (La^{3+}) preserved the growth of TiO$_2$ NPs, and so reduced particle sizes with higher agglomeration are observed. Furthermore, the TEM finding was systematically observed for f-MWCNTs, f-MWCNTs with undoped TiO$_2$, and La^{3+} doped TiO$_2$ NP decorated f-MWCNTs, as shown in Fig. 2(f)–(h). Herein, the introduction of f-MWCNTs into the undoped TiO$_2$ NPs and La^{3+} doped TiO$_2$ NPs favors less extended crystallized domains on f-MWCNTs surfaces, preventing agglomeration and helping more electrolyte ion adsorption and electron transport during electrochemical reactions. Fig. 2(h) shows clear evidence for La^{3+} doped TiO$_2$ NPs favoring less
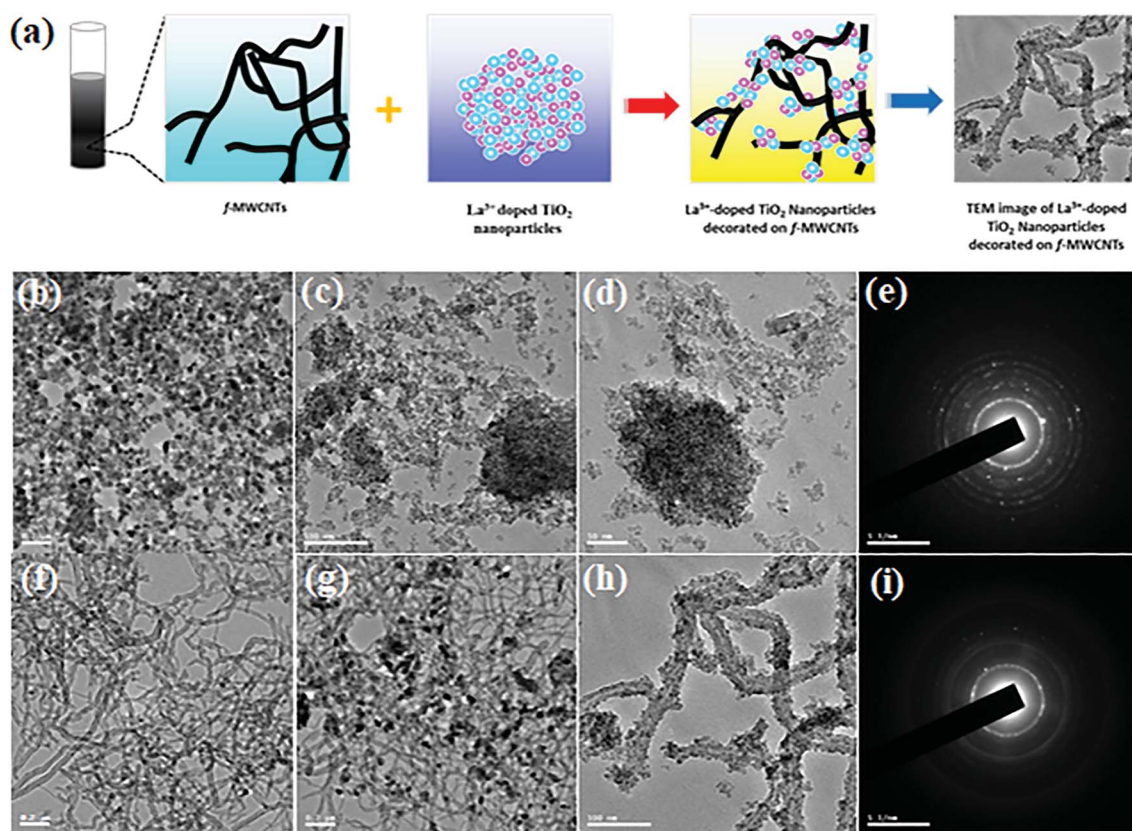
Fig. 2   (a) Schematic illustration of La^{3+} doped TiO$_2$ NP decorated f-MWCNTs, TEM image of (b) TiO$_2$ NPs, (c and d) low and high magnification La^{3+} doped TiO$_2$ NPs, (f) f-MWCNTs, (g) f-MWCNTs/TiO$_2$ NPs, (h) La^{3+} doped TiO$_2$ NP decorated f-MWCNTs, (e and i) SAED for La^{3+} doped TiO$_2$ NPs and La^{3+} doped TiO$_2$ NP decorated f-MWCNTs.

extended crystallized domains on f-MWCNT surfaces while a comparison with undoped TiO_2 reveals that the La^{3+} doped TiO_2 NPs decorated the f-MWCNT active edge surface of the carboxyl group well without any agglomeration. Fig. 2(i) shows the SAED pattern of f-MWCNTs decorated with La^{3+} doped TiO_2 NPs, which shows a ring of polycrystalline nature due to the presence of f-MWCNTs.

Transmission electron microscopy (TEM) images were used to further investigate new insights into La^{3+} doped TiO_2 NP decorated f-MWCNTs. Noticeably, the HR-TEM image shows the rare-earth cation (La^{3+}) doped on the semiconductors of TiO_2 crystals, as shown in Fig. 3(a). The high-resolution TEM image of La^{3+} doped TiO_2 NP decorated f-MWCNTs was analyzed, as displayed in Fig. 3(b). Herein, the La^{3+} doped TiO_2 NPs were decorated on the surface of the f-MWCNTs, as can be seen from Fig. 3(b). The interplanar distance of 0.322 nm corresponds to f-MWCNTs, while the 0.317 and 0.268 nm distances are attributed to the mixed-phase of TiO_2 NPs doped with La^{3+} ions. The prominent interaction between the La^{3+} doped TiO_2 NPs and f-MWCNTs promotes catalytic activity towards an electrochemical sensor.

Moreover, to investigate the elemental distribution of lanthanum (La), titanium (Ti), oxygen (O), and carbon (C) in the La^{3+} doped TiO_2 NP decorated f-MWCNTs, energy dispersive X-ray (EDX) spectroscopy-elemental mapping was carried out, as shown in Fig. 3(c)–(h). These elemental maps exhibit the uniform distribution of the identical elements over the La^{3+} doped TiO_2 NP decorated f-MWCNTs. The EDX spectrum of La^{3+} doped TiO_2 NP decorated f-MWCNTs shows the presence of atomic percentages of lanthanum (La), titanium (Ti), oxygen (O) and carbon (C) without any confirmation of additional impurities, as shown in Fig. 3(i). N_2 adsorption–desorption isotherm analysis was carried out to understand the porous characteristics of f-MWCNTS, TiO_2 NPs, La^{3+} doped TiO_2 NPs, and La^{3+} doped TiO_2 NP decorated f-MWCNTs, as shown in Fig. 4(a)–(d). The specific surface area and pore width were calculated based on the N_2 adsorption–desorption isotherms using the Brunauer–Emmett–Teller (BET) method and the Barrett–Joyner–Halenda (BJH) method; the estimated surface area of f-MWCNTs, TiO_2 NPs, La^{3+} doped TiO_2 NPs, and La^{3+} doped TiO_2 NP decorated f-MWCNTs were calculated to be 124.7675, 141.0792, 167.0390, and 165.1778 m^2 g^{-1}, respectively. These
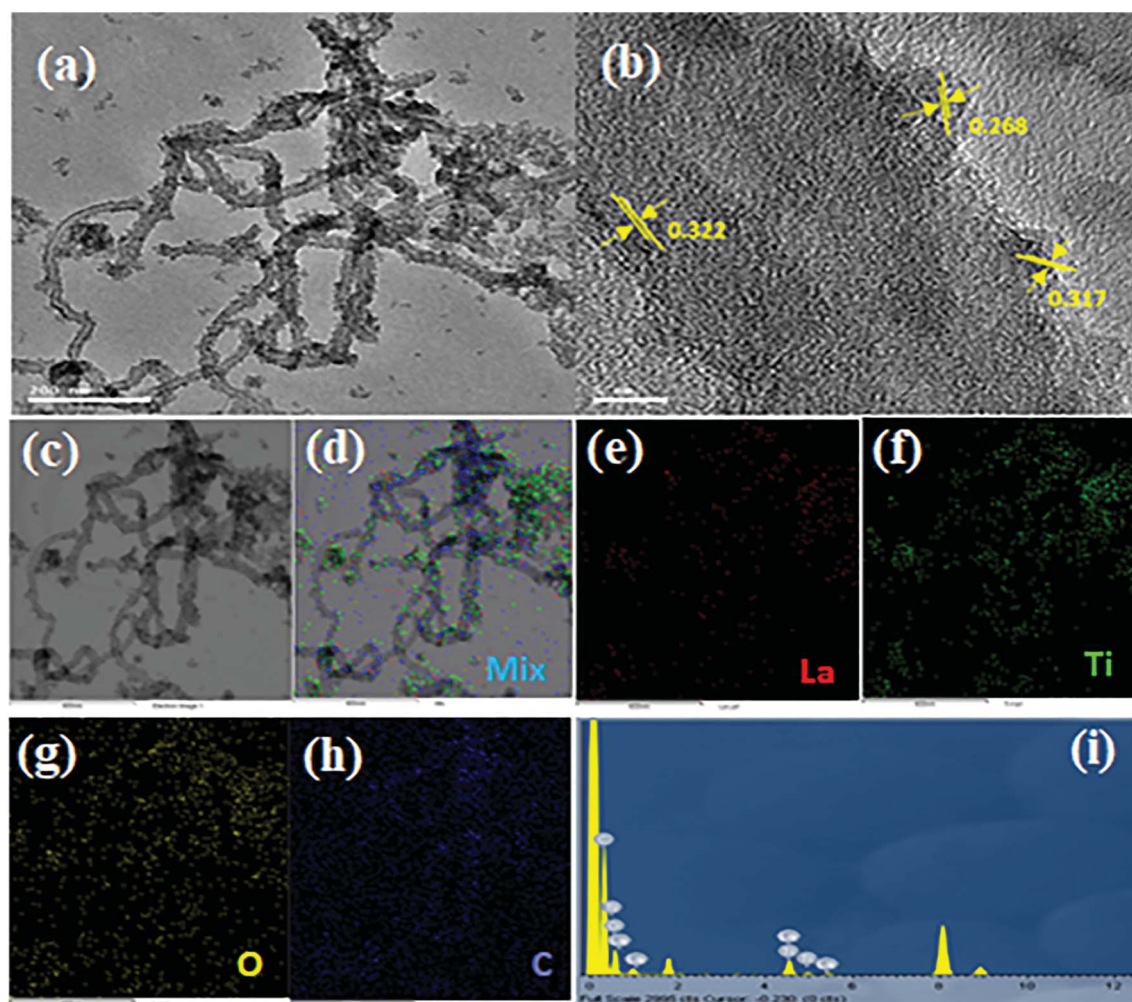

Fig. 3 (a) TEM, (b) HRTEM, (c–h) EDS mapping images, and (i) EDX spectrum of the as-prepared La^{3+} doped TiO_2 NP decorated f-MWCNTs.
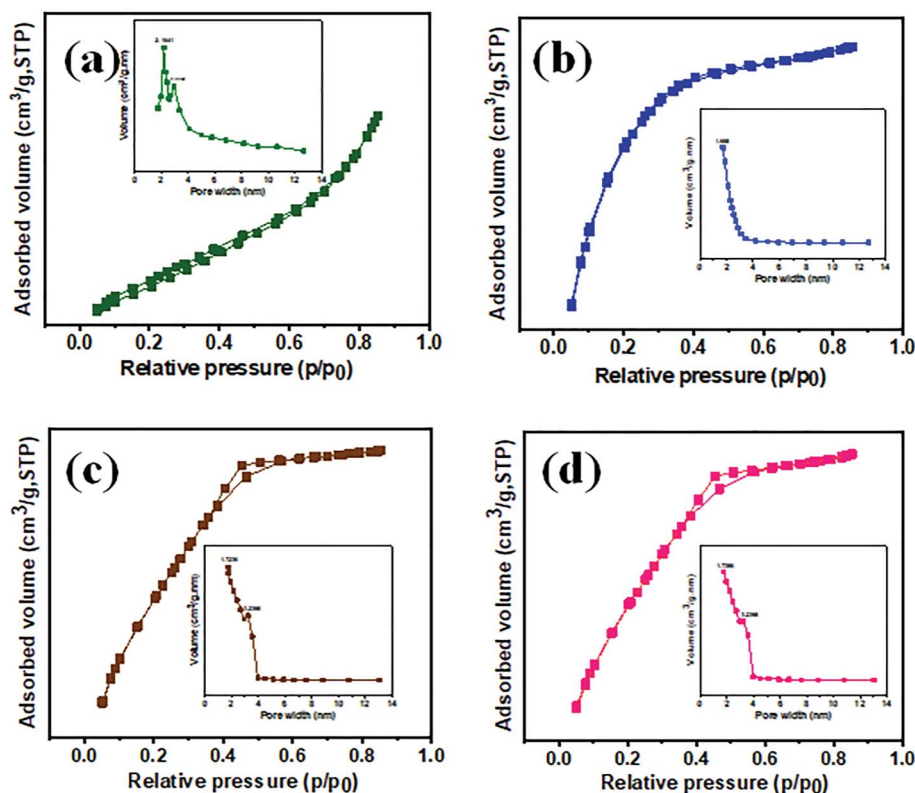
Fig. 4 The N_2 adsorption–desorption isotherms and inset of pore volume of (a) f-MWCNTs, (b) pure-TiO_2 NPs, (c) La^{3+} doped TiO_2 NPs, (d) La^{3+} doped TiO_2 NP decorated f-MWCNTs.

results indicated that La^{3+} doped TiO_2 NPs show a high surface area, and a while after the decoration of f-MWCNTs slight changes were noted, which revealed that the La^{3+} doped TiO_2 NPs attached well on the surface of f-MWCNTs. Moreover, this outcome was effective in making contact with the analyte while electrochemically responding to the electrolyte solution.

X-ray photoelectron spectroscopic (XPS) analysis further confirms the chemical composition and atomic valence states of f-MWCNT$_S$, TiO_2 NPs, La^{3+} doped TiO_2 NPs, and La^{3+} doped TiO_2 NP decorated f-MWCNTs, as shown in Fig. 4. The X-ray photoelectron survey spectra of f-MWCNT$_S$, La^{3+} doped TiO_2, and La^{3+} doped TiO_2 NP decorated f-MWCNTs, as shown in Fig. 5(a), reveal that the signals originated from C, La, Ti, and O. The high-resolution XPS Ti 2p spectrum of TiO_2 NPs can be seen in Fig. 5(b), showing peaks at 459.2 and 464.8 eV for Ti $2p_{3/2}$ and Ti $2p_{1/2}$, respectively. Fig. 5(c) shows the high-resolution XPS spectrum of Ti 2p for La^{3+} doped TiO_2 NPs. The XPS spectra in the core level elements of La^{3+} and Ti^{4+} consist of chemical states, which reveals that the interstitials of Ti^{3+} were observed at 458.1 eV.[37] The shift in the binding energy suggests that La^{3+} may capture electrons from Ti^{4+} states, provoking the reduction of titanium to a low-valence state.[38] The two peaks at 460.2 and 465.4 eV are ascribed to Ti $2p_{3/2}$ and Ti $2p_{1/2}$, respectively, with a slight shift in binding energy, indicating the presence of Ti^{4+} species rather than Ti^{3+} species on the TiO_2 surface of La^{3+} doped TiO_2 NPs, which specifies the strong interaction of the La–O–Ti bond between La^{3+} and the TiO_2 matrix.

Moreover, the high-resolution XPS O 1s spectrum of La^{3+} doped TiO_2 NPs (Fig. 5d) depicts the spectra at 529.3, 531.4, and 534.3 eV, related to there being La–O, Ti–O, and $O–H/OH^-$ bonds on the surface of TiO_2.[39] These pieces of evidence confirm the strong interaction in La–O–Ti bond formation. Furthermore, the high-resolution XPS spectra of f-MWCNTs have peaks at 285.1, 286.1, 287.2, 289.7, and 292.7 eV for graphitic (pure nanotubes), –OH, C=O, O=C–H, and C–C, as shown in Fig. 5(e).[40–42] Herein, the strong intensity peak at 285.1 eV showed the presence of graphitic carbon and an additional weakened bond, indicating more active groups with a COOH structure. In the high-resolution XPS Ti 2p spectra of La^{3+} doped TiO_2 NP decorated f-MWCNTs, shown in Fig. 5(f), the peaks at 459.3 and 465.7 eV are ascribed to Ti $2p_{3/2}$ and Ti $2p_{1/2}$, respectively. Herein, the notable peaks appearing at 464.3 eV of Ti–C, and the interstitials of Ti^{3+} disappeared, revealing that the composite of La^{3+} doped TiO_2 NPs was well decorated on the active functional sites (–COOH) of f-MWCNTs. In the high-resolution f-MWCNT decorated La^{3+} doped TiO_2 XPS spectrum of La 3d, shown in Fig. 5(g), the two peaks at 832.7 and 855.1 eV are assigned to two spin orbits of La $3d_{5/2}$ and La $3d_{3/2}$, respectively. Moreover, the other two peaks at 837.8 and 859.8 eV are La 3d satellite peaks. As we know, there is a general agreement in the literature that the split-spin orbit reflects states with configurations $[3d^9]^{hole} 4f^0$ L and $[3d^9]^{hole} 4f^1 [L]^{hole}$, where L indicates the oxygen ligand.[43] The XPS spectra of La 3d show the satellite peaks at higher energy sides, which caused by
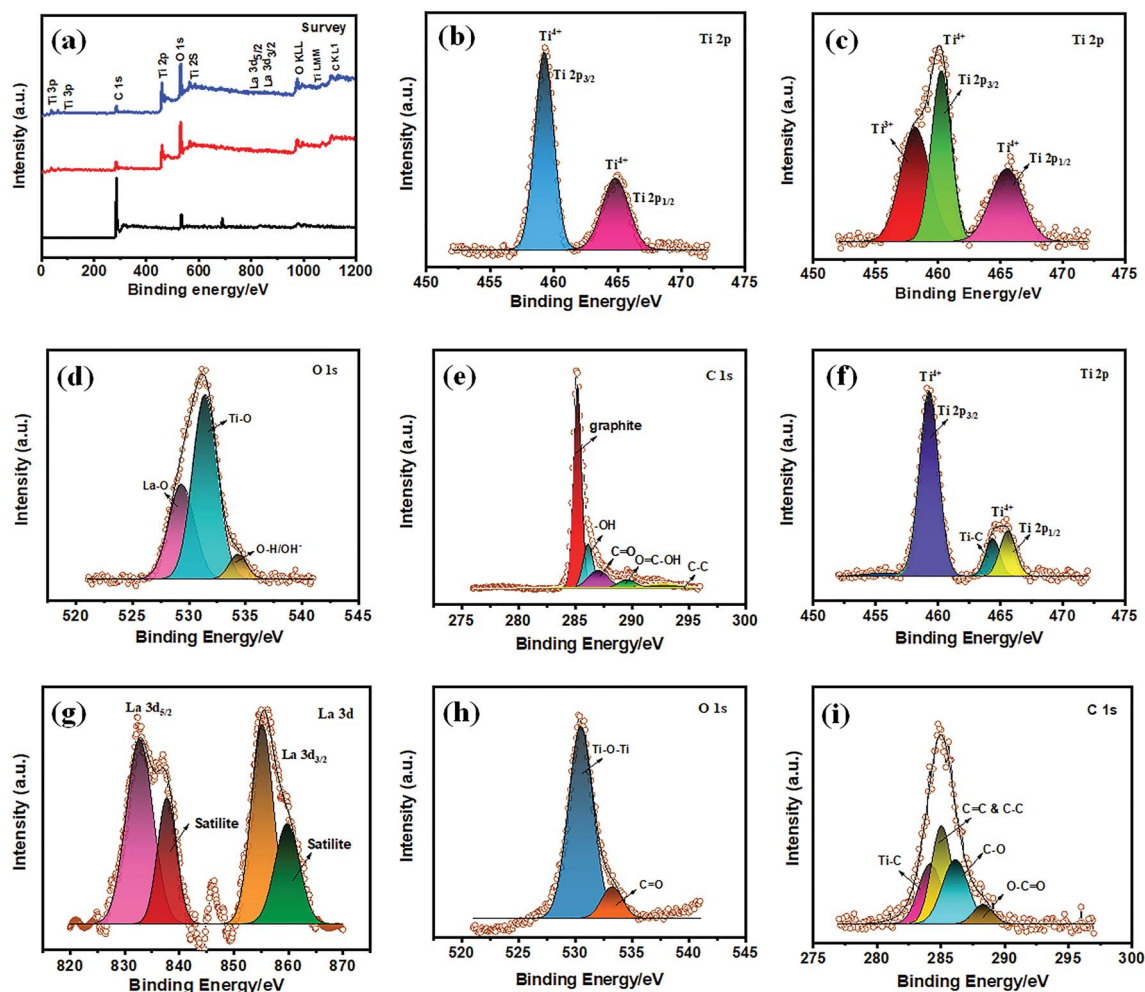
Fig. 5 (a) X-ray photoelectron survey spectrum of f-MWCNT$_S$, La^{3+} doped TiO$_2$ NPs and La^{3+} doped TiO$_2$ NP decorated f-MWCNTs, (b and c) high-resolution XPS spectrum of Ti 2p of TiO$_2$ NPs and La^{3+} doped TiO$_2$ NPs, (d) XPS O 1s spectrum of La^{3+} doped TiO$_2$ NPs, (e) C 1s spectrum of f-MWCNT$_S$, (f–i) high-resolution XPS spectrum of (f) Ti 2p (g) La 3d, (h) O 1s, (i) C 1s for La^{3+} doped TiO$_2$ NP decorated f-MWCNTs.

the f^0 domination at lower binding energy and reflected to be f^1 of La, indicating the presence of La into the TiO$_2$ matrix. In the high-resolution XPS spectrum of O 1s, shown in Fig. 5(h), the two O 1s peaks centered at 530.3 and 533.3 eV are assigned to Ti–O–Ti, and C=O, and associated with oxygen defects in the TiO$_2$ matrix caused by oxygen vacancies. From the chemical state of the C 1s spectrum (Fig. 5(i)) arise the peaks at 284.1, 285.0, 286.1 and 288.3 eV, which implies the presence of Ti–C, C–C & C=C, C–O, and O–C=O, respectively.[44] These results indicate that the La^{3+} doped TiO$_2$ NPs were successfully decorated on the f-MWCNTs.

3.2. Electrochemical characterizations

3.2.1. Electrocatalysis of modified electrodes. The first task was to analyze and estimate the electrocatalytic response of the individual modified sensors, which were systematically investigated with a 0.1 M KCl; 5 mM [Fe(CN)$_6$]$^{3-/4-}$ redox probe electrolyte. The electrochemical performances of bare GCE, TiO$_2$NPs/GCE, f-MWCNTs/GCE, f-MWCNT decorated TiO$_2$/GCE, La^{3+} doped TiO$_2$/GCE, and La^{3+} doped TiO$_2$ NP decorated f-

MWCNTs/GCE can be seen in Fig. 6(a). From observation of Fig. 6(a), the La^{3+} doped TiO$_2$ NP decorated f-MWCNTs/GCE shows a well-defined redox peak current and high electron transfer capability, which are systematically compared with other modified electrodes: f-MWCNT decorated TiO$_2$/GCE, f-MWCNTs/GCE, La^{3+} doped TiO$_2$ NPs/GCE, TiO$_2$NPs/GCE, and bare GCE. Thus, La^{3+} doped TiO$_2$ NP decorated f-MWCNTs/GCE modified electrochemical sensors act as efficient electron mediators owing to their excellent electrical conductivity and high specific surface area on the modified GCE surface. The peak-to-peak potential (ΔE_p) separations of bare GCE, f-MWCNTs/GCE, TiO$_2$NPs/GCE, f-MWCNT decorated TiO$_2$/GCE, La^{3+} doped TiO$_2$ NPs/GCE and La^{3+} doped TiO$_2$ NP decorated f-MWCNTs/GCE are 122.8, 108.5, 81.9, 82, 112.9 and 80.9 mV, respectively. The redox peak current of La^{3+} doped TiO$_2$ NP decorated f-MWCNTs/GCE is significantly lower than that of bare GCE, f-MWCNTs/GCE, TiO$_2$ NPs/GCE, f-MWCNT decorated TiO$_2$/GCE, or La^{3+} doped TiO$_2$ NPs/GCE, and shows a well-defined peak current with a noticeable negative peak shift compared to other modified GCE electrodes. Moreover, the La^{3+}
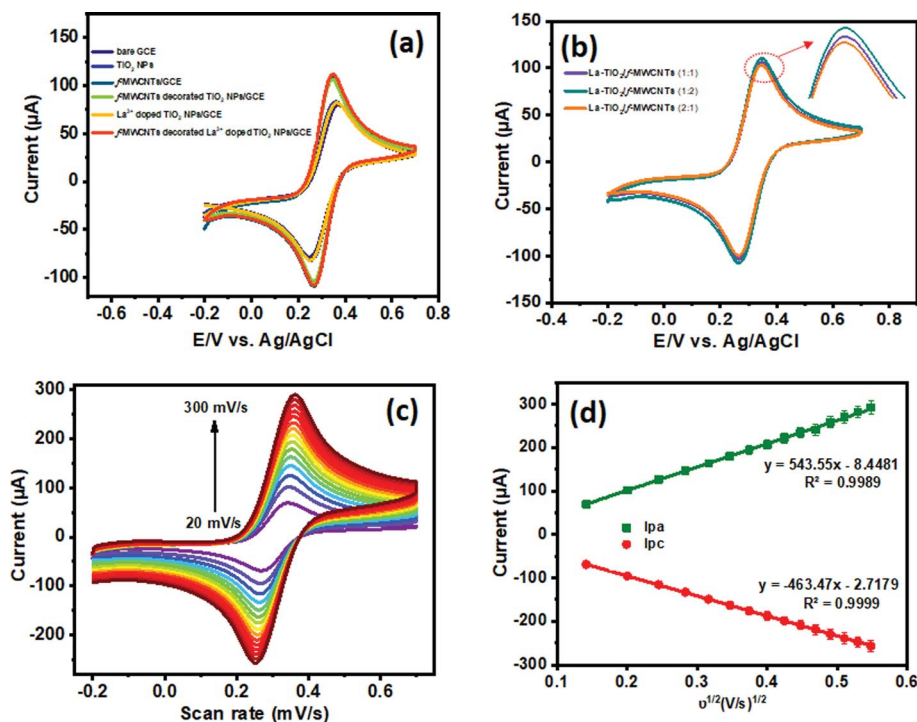
Fig. 6 (a) Cyclic voltammetry of 0.1 M-KCl; 5 mM $[Fe(CN)_6]^{3-/4-}$ redox probe at bare GCE, f-MWCNTs/GCE, TiO_2 NPs/GCE, f-MWCNT decorated TiO_2/GCE, La^{3+} doped TiO_2/GCE and La^{3+} doped TiO_2 NP decorated f-MWCNTs/GCE, (b) CV responses of different ratios (1 : 1, 1 : 2, and 2 : 1) of La^{3+} doped TiO_2 NP decorated f-MWCNTs/GCE nanocomposite in the presence of 0.1 M KCl; 5 mM $[Fe(CN)_6]^{3-/4-}$ redox probe, (c) CVs obtained for La^{3+} doped TiO_2 NP decorated f-MWCNTs/GCE nanocomposite with different scan rates (20–300 mV s^{-1}), (d) corresponding calibration plots for current *vs.* $\nu^{1/2}$ (mV s^{-1})$^{1/2}$.

doped TiO_2 NP decorated f-MWCNTs/GCE exhibits an I_{pa}/I_{pc} value of 1.03, which implies that the $[Fe(CN)_6]^{3-/4-}$ redox probe was quasi-reversible. The La^{3+} doped TiO_2 NP decorated f-MWCNTs/GCE obtained definite peak current responses compared to other modified sensors, such as TiO_2 NPs/GCE, La^{3+} doped TiO_2 NPs/GCE, or bare GCE, which demonstrates that La^{3+} doped TiO_2 NPs are very attracted to the surface of f-MWCNTs. These factors must be strongly influenced by the current enhancement with fast electron transfer in the electrode–electrolyte system. These results demonstrate that the La^{3+} doped TiO_2 NP decorated f-MWCNTs/GCE exhibits active electron transfer ability, excellent electrical conductivity, and high surface area on the GCE electrode surfaces. Fig. 6(b) shows the different ratios (1 : 1, 1 : 2, and 2 : 1) of La^{3+} doped TiO_2 NP decorated f-MWCNTs modified GCE that were used to analyze the electrode surface catalytic activity in the presence of a $[Fe(CN)_6]^{3-/4-}$ redox probe at 50 mV s^{-1}. The La^{3+} doped TiO_2 NP decorated f-MWCNT modified GCE (1 : 2 ratio) shows much more electron transfer capability compared to other ratios. Due to this factor, we preferred a (1 : 2) ratio for the modified electrode in the electrocatalytic analysis. Furthermore, the electrochemically active surface area of the modified electrode was calculated from the Randles–Sevcik equation, as can be seen in eqn (2):[45]

$$i_p = 2.69 \times 10^5 n^{3/2} A D^{1/2} C \nu^{1/2} \qquad (2)$$

where i_p is the peak current (A), A is the electrochemically active area (cm^2), n is the number of electrons transferred, C is the concentration of electroactive species (mol cm^{-3}), D is the diffusion coefficient (cm^2 s^{-1}), and $\nu^{1/2}$ is the scan rate (V s^{-1}). Thereby, the redox properties of La^{3+} doped TiO_2 NP decorated f-MWCNT modified GCE were observed in the presence of a redox probe ($[Fe(CN)6]^{3-/4-}$) at various scan rates ranging from 20 to 300 mV s^{-1}, as shown in Fig. 6(c). Fig. 6(d) shows the corresponding calibration plot for current *vs.* $\nu^{1/2}$ (mV s^{-1})$^{1/2}$. From the calculation, the electrochemically active surface area of the GCE modified electrode was calculated to be 1469.0 cm^2.

The electrochemical sensor has a vital role in monitoring the type and level of pollution. Notably, the sensing performance of a chemically modified electrode depends upon its electrode–electrolyte activity in the presence and absence of the analyte. Herein, we use paraoxon-ethyl (PE) for the electrocatalytic analysis of the sensing performance of the modified electrode, in order to monitor the pollutant in an environmental ecosystem. Fig. 7(a) and (b) show the CV electrocatalytic behavior of bare GCE, TiO_2 NPs/GCE, f-MWCNTs/GCE, f-MWCNT decorated TiO_2 NPs/GCE, La^{3+} doped TiO_2 NPs/GCE and La^{3+} doped TiO_2 NP decorated f-MWCNTs/GCE in the absence and presence of PE (50 μM), evaluated with 0.05 M phosphate buffer (PB) solution at a scan rate of 50 mV s^{-1}. Fig. 7(a) displays the CVs of unmodified and modified GCE electrodes (1 mg mL^{-1}; 6 μL), wherein the modified electrodes of f-MWCNTs/GCE, f-MWCNT decorated TiO_2 NPs/GCE, and La^{3+} doped TiO_2 NP decorated f-

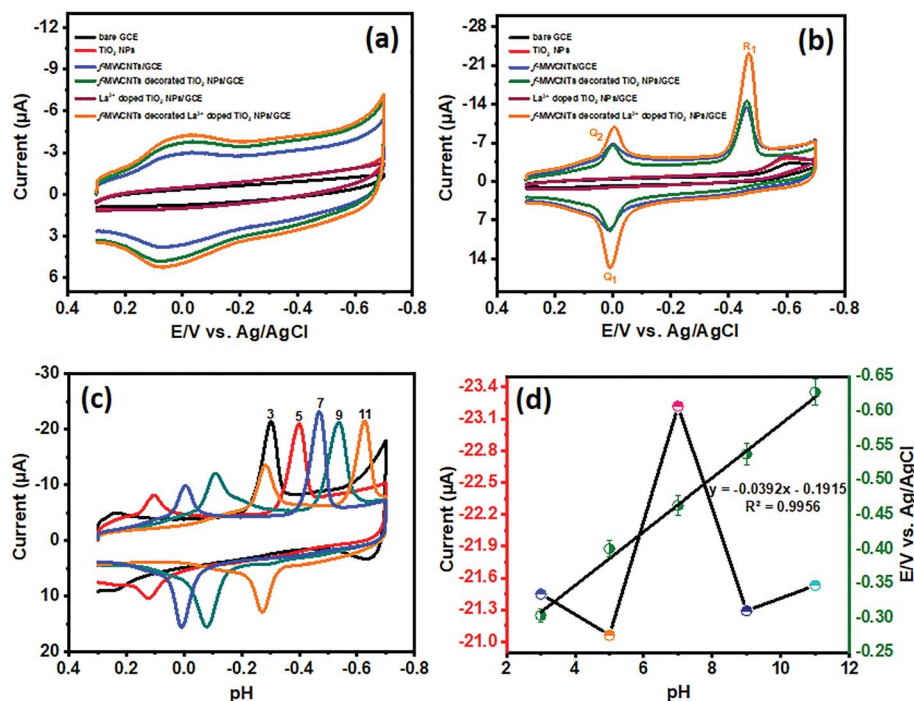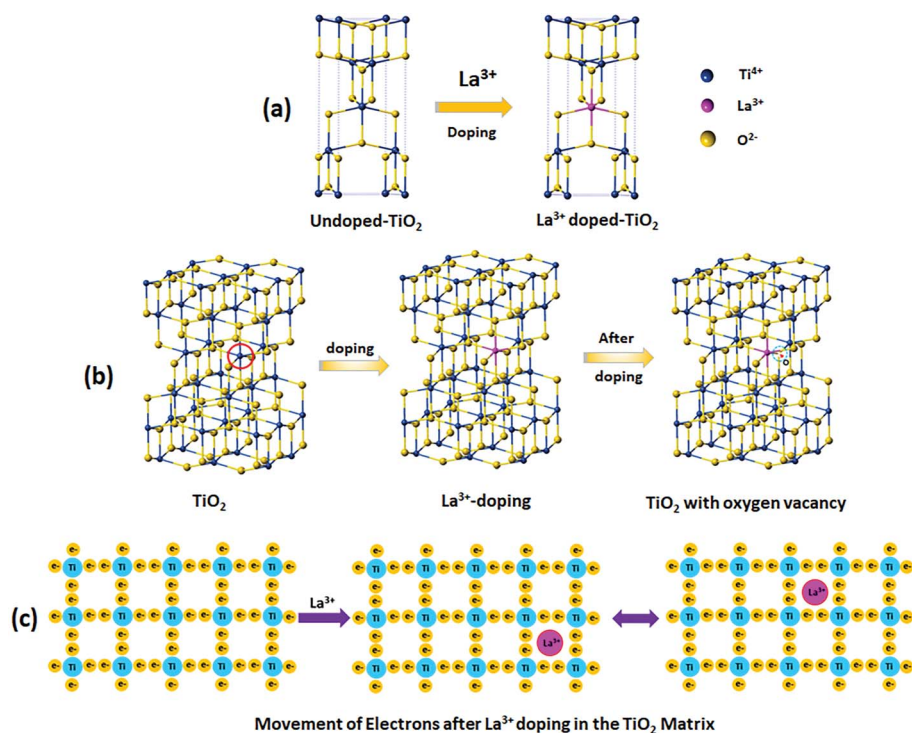**Fig. 7** (a and b) CVs of bare GCE, TiO_2 NPs, f-MWCNTs/GCE, f-MWCNT decorated TiO_2 NPs/GCE, La^{3+} doped TiO_2 NPs/GCE and La^{3+} doped TiO_2 NP decorated f-MWCNTs/GCE in the absence and presence of PE (50 μM), (c) CVs of the reduction of PE (50 μM) at f-MWCNT decorated TiO_2 NPs/GCE at various pH values ranging from 3.0 to 11.0, and (d) the corresponding PE reduction peak current and potential responses vs. different pH values.

MWCNTs/GCE show a high background capacitance. It can be seen from Fig. 7(a) that the modified electrodes of TiO_2 NPs/GCE and La^{3+} doped TiO_2 NPs/GCE show very low capacitance, which suggests that there is not that much corresponding increase in capacitance when La^{3+} is introduced into the TiO_2 NPs at a scan rate of 50 mV s^{-1}. In particular, the

Scheme 3 (a) 3D schematic unit cell representation of undoped TiO_2 and La^{3+} doped TiO_2 crystal structures, (b) the substitution of Ti^{4+} ions by La^{3+} ions in the TiO_2 matrix, (c) 2D schematic representation of the movement of electrons in the TiO_2 matrix after La^{3+} doping.

carbon materials are much attracted, resulting in a greater surface area, and the capacitance of f-MWCNTs/GCE showed a similar response to f-MWCNT decorated TiO$_2$ NPs/GCE and La^{3+} doped TiO$_2$ NP decorated f-MWCNTs/GCE electrode. Thus, these indicate the synergetic effect generated on the f-MWCNT decorated TiO$_2$ and La^{3+} doped TiO$_2$ NP modified GCE electrode. Notably, the La^{3+} doped TiO$_2$ NP decorated f-MWCNT modified GCE electrode exposes a highly active surface to the electrolyte, and the intermediate layer of f-MWCNTs ensures super electrical conductivity towards the electrode–electrolyte system. The layered structures of f-MWCNTs facilitate fast electron transportation and ion diffusion within the modified electrode, which is helpful for the use of the electroactive materials, improving their capacitive performance and enhancing their catalytic activity.

Furthermore, for the unmodified and modified GCE electrodes evaluated with PE (50 μM), the electrocatalysis of PE recorded with 0.05 M PB solution at a scan rate of 50 mV s^{-1}, and the CVs are shown in Fig. 7(b). The rate of electro-reduction behavior of PE was used to further evaluate the unmodified and modified electrodes with onset reduction potentials (E_{onset}). The onset reduction potentials were −0.5084 V for bare GCE, −0.4011 V for f-MWCNTs/GCE, −0.4988 V for TiO$_2$ NPs/GCE, −0.4045 V for f-MWCNT decorated TiO$_2$/GCE, −0.504 V for La^{3+} doped TiO$_2$/GCE, and −0.4097 V for La^{3+} doped TiO$_2$ NP decorated f-MWCNTs/GCE. The electrocatalytic activity for PE validation was considered in terms of activation potential ($E_p - E_{onset}$). The bare GCE, f-MWCNTs/GCE, TiO$_2$ NPs/GCE, f-MWCNT decorated TiO$_2$/GCE, La^{3+} doped TiO$_2$/GCE, and La^{3+} doped TiO$_2$ NP decorated f-MWCNTs/GCE show reductions in peak potential of 113.5, 62.8, 105.6, 58.6, 96.9 and 53.4 mV from the onset potential. Thus, these observations revealed that La^{3+} doped TiO$_2$ NP decorated f-MWCNTs/GCE gives the most satisfying electrocatalytic performance for PE in terms of reduction potential.

3.2.2. Mechanism of PE reduction. The mechanism of PE reduction was recently demonstrated by Raj Karthik *et al.* by analysis of the electrochemical sensor.[6] Fig. 7(b) shows the experimental CV results of PE reduction and redox reaction at the La^{3+} doped TiO$_2$ NP decorated f-MWCNT modified GCE recorded at a scan rate of 50 mV s^{-1}, which is summarized as a detailed mechanistic overview in Scheme 4. In detail, the electrochemical behavior of PE at the GCE modified electrode shows the reduction peak current (R$_1$) at −0.4707 V. This observed peak initially related to the (irreversible) direct (4 e$^-$; 4H$^+$) electron transfer process, which converts the paraoxon-ethyl (PE) to diethyl(4-hydroxyamino) phenyl phosphate (system I). The clear evidence of Fig. 7(b) shows that no oxidation peak was observed corresponding to the reduction peak of R$_1$ (system I), which revealed that R$_1$ is a direct (irreversible) electron transfer process. Moreover, the redox couples at 0.0083 V (Q$_1$) and 0.0049 V (Q$_2$) are related to the
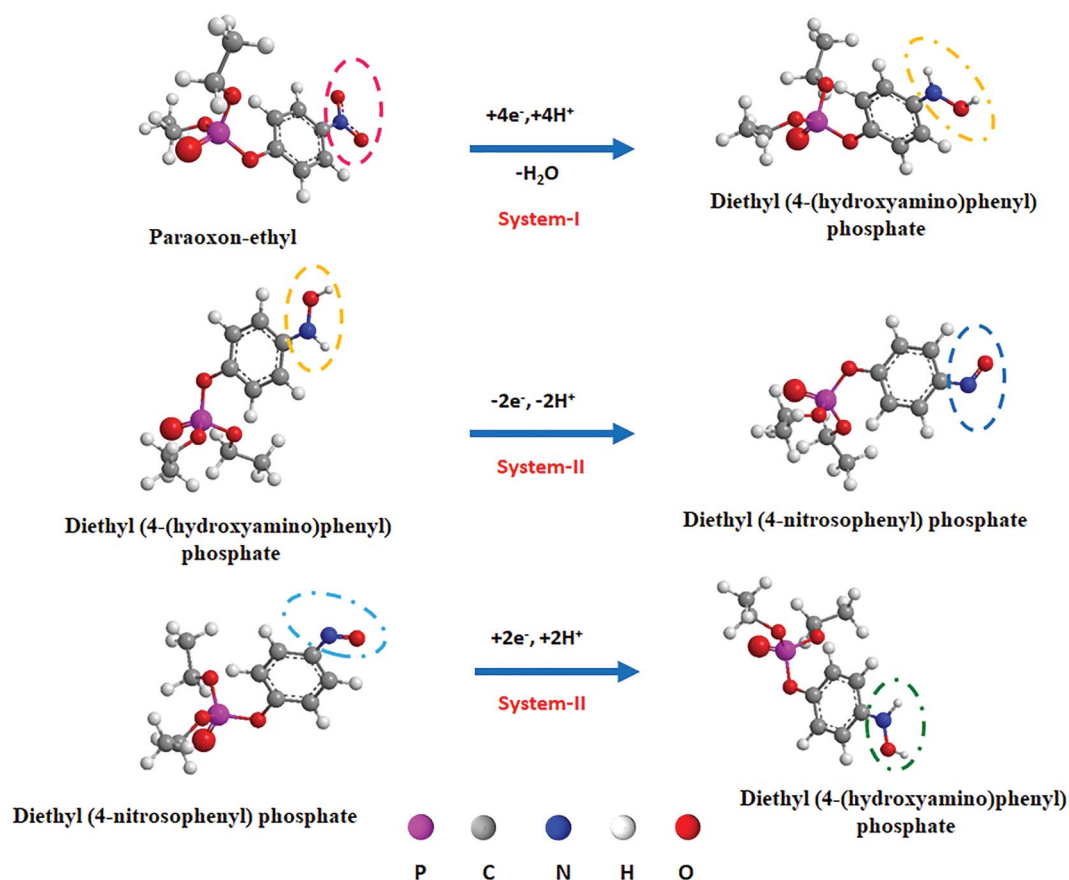
Scheme 4 A plausible mechanism for the electrochemical reduction of PE.
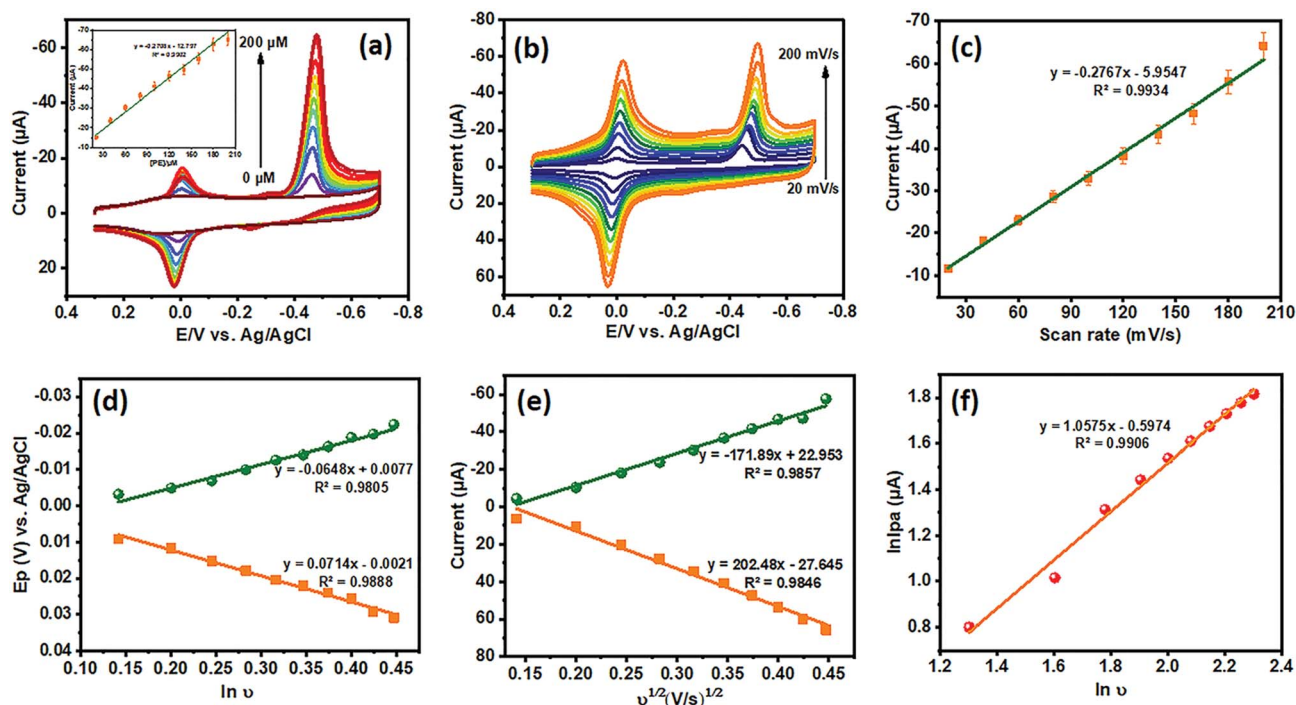
Fig. 8 (a) CVs of PE at the La^{3+} doped TiO_2 NP decorated f-MWCNT modified GCE for different concentrations from 0 to 200 μM, and (b) the corresponding different cathodic peak current *vs.* concentration (Ag/AgCl), (c) CVs of the La^{3+} doped TiO_2 NP decorated f-MWCNT modified GCE in 0.05 M PB (pH 7) containing PE (50 μM) for different scan rates (20 to 200 mV s^{-1}), (d) corresponding cathodic peak current responses *vs.* scan rate (e) peak current (Q_1 and Q_2) *vs.* square root of scan rate, (f) log of peak current (I_{pa}; Q_1) plotted *vs.* the natural logarithm of scan rate (ln *v*).

two electron (e^-) and two proton (H^+) transfer process at the hydroxylamine group (systems II and III). Notably, Fig. 7(b) shows the reversible peaks of diethyl (4-nitrosophenyl) phosphate from diethyl (4-(hydroxyamino)phenyl) phosphate, respectively. Furthermore, the obtained cathodic peak (R_1) response of PE is crucial compared with Q_2, which is related to the direct and fast electron transfer process. For the choice of an La^{3+} doped TiO_2 NP decorated f-MWCNT modified GCE being favorable to detect PE, it has a lower potential (-0.4707 V) compared to the value from R. Karthik *et al.* (-0.62)[6] previously reported in the literature.

3.2.3. Effect of electrolyte, concentration, and kinetics. One of the essential determinants of electrolytes is a prominent factor for the catalytic activity of PE in the oxidation and reduction processes at different pH values, which are responsible for the catalytic behavior of La^{3+} doped TiO_2 NP decorated f-MWCNT modified GCE at 50 mV s^{-1}. The CV profiles of electrocatalytic behavior for the La^{3+} doped TiO_2 NP decorated f-MWCNT modified GCE in different aqueous electrolytes (with different pH values) were recorded, and are depicted in Fig. 7(c). This signified that with an increase in pH, the reduction peak potentials shifted towards the positive direction, which suggests that protons were involved in the electrode process. As displayed in Fig. 7(c), the peak current occurred for La^{3+} doped TiO_2 NP decorated f-MWCNT modified GCE at 50 μM (PE) at 50 mV s^{-1}, while a shift in the peak was observed towards the negative direction between the potentials of 0.2 and -0.7 V. To verify the cathodic peak current responses of 50 μM (PE) at the

La^{3+} doped TiO_2 NP decorated f-MWCNT modified GCE at different pH (pH values = 3.0, 4.0, 7.0, 9.0, and 11.0), the peak current (I_{pc}) was plotted against pH, as shown in Fig. 7(d). The cathodic peak current responses of PE show that the neutral medium of PB (pH 7) shows the highest peak current responses compared with others under optimal conditions. Therefore, pH 7 was chosen for all the analytical electrochemical studies. Subsequently, a linear plot of pH *vs.* E_{pc} was constructed, and the peak potential was found to be linear with pH, obeying the Nernst equation (-0.0392 V/pH; $R^2 = 0.9956$), as displayed in Fig. 7(d).

$$E_p = E^0 - (m/n)0.059\text{pH} \qquad (3)$$

where E^0 is the standard potential, and m and n are the numbers of protons and electrons. From the linear plot of E_{pc} (V) *vs.* pH, the numbers of electrons and protons are equally involved on La^{3+} doped TiO_2 NP decorated f-MWCNT modified GCE for the detection of PE.

The dependence of peak current of PE was analyzed *via* different concentrations in 0.05 M PB (pH 7) using cyclic voltammetry (CV). To ascertain the effect of PE at the La^{3+} doped TiO_2 NP decorated f-MWCNT modified GCE, the PE concentration was increased to 200 μM, as shown in Fig. 8(a). As displayed in Fig. 8(a), the peak current responses of PE increased gradually when the concentration of PE was increased. Thus, these results suggested that the concentration of PE was directly proportional to the concentration of the analyte (PE). The

corresponding peak current responses (with the linear correlation coefficient $R^2 = 0.9902$) are shown in the inset of Fig. 8(a).

The electrochemical kinetics of PE were analyzed *via* different scan rates (20 to 200 mV s^{-1}) at the La^{3+} doped TiO$_2$ NP decorated f-MWCNT modified GCE, as displayed in Fig. 8(b). Initially, the reduction peak (R$_1$) of PE at 0.4456 V was observed on the modified electrode at an initial scan rate of 20 mV s^{-1}, then with a continuous scan rate the peak potential moved slightly towards the negative side, because of the internal resistance of the adsorbed products. Thus, these irreversible reduction processes were associated with the transfer of 4e$^-$; 4H$^+$, as addressed earlier. Noticeably, the cathodic peak current (R$_1$) of PE increased linearly with an increase in the scan rate; see the corresponding linear calibration plot shown in Fig. 8(c). This linear plot relates to the linear regression equation, shown in eqn (4). Furthermore, after the reduction in PE (peak R$_1$), no corresponding oxidation peak is observed, suggesting that the direct electron transfer (4e$^-$; 4H$^+$) on the La^{3+} doped TiO$_2$ NP decorated f-MWCNT modified GCE at different scan rates.

$$I_{pc} = -0.2767(PE) - 5.9547 \ (R^2 = 0.9934) \tag{4}$$

Fig. 7(b) shows the active redox peaks (Q$_1$/Q$_2$) of diethyl (4-nitrosophenyl)phosphate from diethyl (4-(hydroxyamino) phenyl)phosphate; thereby this was related to the c 2e$^-$; 2H$^+$ transfer process. Fig. 8(d) show the peaks of Q$_1$ and Q$_2$ of potential (E_p) plotted against the natural logarithm of scan rate

(ln ν). Moreover, Fig. 8(e) shows the resultant peak current (Q$_1$ and Q$_2$) plotted against the square root of the scan rate with the linear correlation coefficient (I_{pc}; $R^2 = 0.9857$ and I_{pa}; $R^2 = 0.9846$) followed by the linear regression equation. The results indicate that the electrochemical redox behavior of Q$_1$ and Q$_2$ (systems II and III) at the La^{3+} doped TiO$_2$ NP decorated f-MWCNT modified GCE electrode was a reversible adsorption-controlled process,[46] which is favorable for quantitative applications. Furthermore, the peak potential (E_{pa}: Q$_1$) plotted *vs.* the natural logarithm of scan rate (ln ν) shows a slope of 1.05 ($R^2 = 0.9906$) for the anodic peak (Q$_1$) of PE, as shown in Fig. 8(f). According to the kinetic theory of the electrode reaction (eqn (5)),[47] the slope values of log I_{pa} *vs.* log(mV s^{-1}) should be 0.5 V and 1 V for pure diffusion and adsorption-controlled processes.

$$I_{pa} = A\nu^x \tag{5}$$

where I_{pa} is the oxidation peak current (A), ν is the scan rate (mV s^{-1}), and x corresponds to -0.5, and 1, respectively. Moreover, the electron-transfer kinetic parameters, such as electron-transfer coefficient (α) and apparent charge-transfer rate constant (K_s) for the reversible processes of Q$_1$ and Q$_2$, calculated from the Laviron equation (eqn (6)–(10)), gave values of 0.8201 and 1.1038 s^{-1}, respectively.
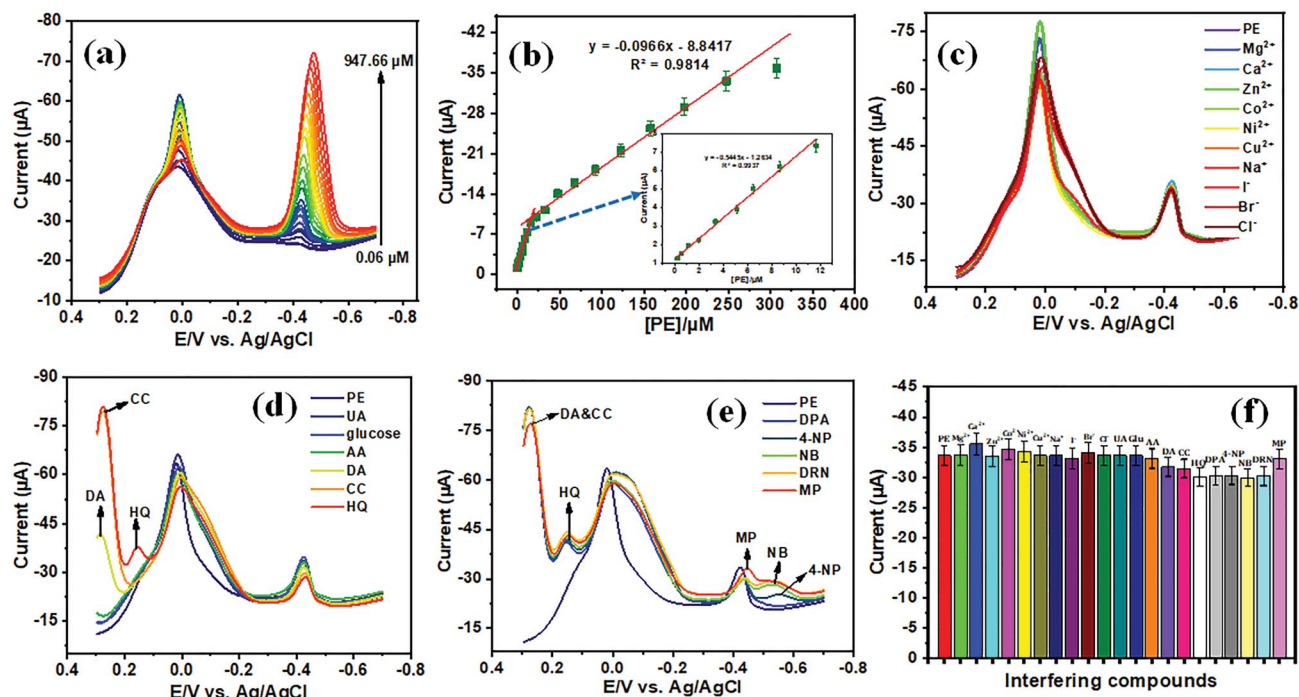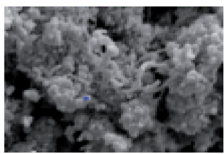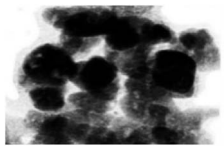
$$E_{pa} = E^0 + A \ln \nu \tag{6}$$

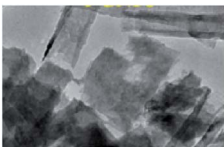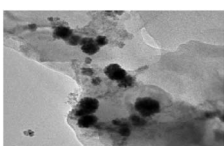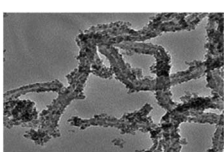**Fig. 9** (a) DPV responses of the La^{3+} doped TiO$_2$ NP decorated f-MWCNT modified GCE for PE detection, (b) corresponding linear current responses *vs.* concentration of PE, (c) DPV response at the La^{3+} doped TiO$_2$ NP decorated f-MWCNT modified GCE with the addition of 10 μM PE and 200 μM concentrations of interfering species such as Mg^{2+}, Ca^{2+}, Zn^{2+}, Fe^{2+}, Co^{2+}, Ni^{2+}, Cu^{2+}, Na$^+$, I$^-$, Br$^-$, and Cl$^-$, (d) the continuous addition of 100 μM of biological substances of uric acid (UA), glucose (Glu), ascorbic acid (AA), dopamine (DA), caffeic acid (CA), catechol (CC), and hydroquinone (HQ), (e) 30 μM excess of nitro-aromatic and pesticides containing compounds of diphenylamine (DPA), 4-nitrophenol (4-NP), nitrobenzene (NB), diuron (DRN), and methyl parathion (MP), (f) the calibration plot of I_{pc} *vs.* interfering compounds.

Table 1 Comparison of the electrocatalytic performance of the La^{3+} doped TiO$_2$ NP decorated f-MWCNT modified GCE electrode towards PE detection with previously reported sensors

Modified electrodes/methods	Morphology	Sensitivity (μA μM^{-1} cm^{-2})	Linear range (μM)	LOD (μM)	Ref.
CP/OPH (amperometric)	—	0.0014	4.6–46.0	0.9	50
CLEC-OPH (amperometric)	—	0.025	0.50–2.0	0.314	51
CNT/OPH (amperometric)	—	0.025	0.25–4.0	0.15	52
BSA@Cu-SWCNT (SWV)		—	0.05–35	0.0128	53
Gr@NiFeSP/GCE (SWV)		—	0.012–10	0.0037	54
GCE/YbM/f-CNFs (amperometric)		2.87	0.01–12 & 14–406	0.002	6
PdNPs/BNHJ/GCE (LSV)		2.23	0.01–210	0.003	49
f-MWCNTs/La^{3+}–TiO$_2$/GCE (DPV)		7.6690	0.06–11.66 & 11.66–307.66	0.0019	This work

$$E_{pc} = E^0 - B \ln \nu \qquad (7)$$

$$A = RT/(1 - \alpha)nF; \; B = RT/\alpha nF$$

$$E_{pa} = E^0 + (RT|(1 - \alpha)nF)\ln \nu \qquad (8)$$

$$E_{pc} = E^0 - \left(\frac{RT}{\alpha nF}\right)\ln \nu \qquad (9)$$

$$\log K_s = \alpha \log(1 - \alpha) + (1 - \alpha)\log \alpha - \log \frac{RT}{nF\nu}$$
$$- \frac{\alpha(1 - \alpha)nF\Delta E_p}{2.303 RT} \qquad (10)$$

where E^0 is the formal redox potential, n is the number of transferred electrons, ν is the scan rate, ΔE_p is the peak-to-peak potential separation, and the other symbols have their usual significance.

3.2.4. Analytical performance. The differential pulse voltammetry (DPV) response of the La^{3+} doped TiO$_2$ NP decorated f-MWCNT modified GCE electrode was recorded to determine the PE sensing performance by successive additions of PE concentrations (Fig. 9(a)); where the strength of PE increased

from 0.06 to 947.66 μM in the presence of 0.05 M PB (pH 7) in a fixed potential window (0.3 to −0.7). Under the selected conditions, the initial concentration of PE (up to 11.66 μM) shows that the cathodic peak (R$_1$) current increases linearly with a linear correlation coefficient of 0.9937, as shown in the inset of Fig. 9(b). For the continuous addition, we observed the reduction peak current with satisfactory linearity from 11.66 to 307.66 μM with a linear correlation coefficient of $R^2 = 0.9814$, as shown in Fig. 9(b). Conversely, the cathodic peak current of PE (Q$_2$) decreased when a higher concentration was reached; this implies that there are no more active sites, which means that due to saturation of PE, the kinetic limitation has been reached on the modified electrode. Furthermore, to estimate the PE performance of the designed electrochemical sensor, it was utilized to consider the sensitivity of the La^{3+} doped TiO$_2$ NP decorated f-MWCNT modified GCE electrode in terms of the limit of detection (LOD) and limit of quantification (LOQ) for PE detection. DPV is a pulse voltammetry technique that supports an essential function during electrochemical sensing while analyzing traditional sweep systems. The LOD and LOQ of the

PE were calculated from the slope value of the calibration plot according to eqn (11) and (12).[48]

$$LOD = 3 \times SD/B \qquad (11)$$

$$LOQ = 10 \times SD/B \qquad (12)$$

where SD is the standard deviation of the blank, B is the calibration sensitivity that is the slope of the linear plot of concentration $vs.$ current. Accordingly, LOD and LOQ were found to be 0.0019 μM and 0.0065 μM. It is worth noting that the sensitivity to PE at the La^{3+} doped TiO$_2$ NP decorated f-MWCNT modified GCE electrode was found to be 7.6690 μA μM^{-1} cm^{-1}; which is comparable with values lately reported in the literature, such as YbM/f-CNFs/GCE (2.87 μA μM^{-1} cm^{-1})[6] and Pd NPs/BNHJ/GCE (2.33 μA μM^{-1} cm^{-1}).[49] These comparison data further indicate that the La^{3+} doped TiO$_2$ NP decorated f-MWCNT modified GCE electrode shows remarkable electrocatalytic action towards the reduction of PE, and these results are highly comparable with a previously reported PE sensor (Table 1).[6,50–54] These observed data further indicate that the La^{3+} doped TiO$_2$ NP decorated f-MWCNT modified GCE electrode shows very remarkable electrocatalytic action towards PE detection.

3.2.5. The selectivity of the La^{3+} doped TiO$_2$ NP decorated f-MWCNT modified GCE for PE sensing. Selectivity is known to be another attribute of a proposed sensor; therefore, the DPV of the La^{3+} doped TiO$_2$ NP decorated f-MWCNT modified GCE electrode was examined for PE (10 μM) with some non-specific cations including Mg^{2+}, Ca^{2+}, Zn^{2+}, Fe^{2+}, Co^{2+}, Ni^{2+}, Cu^{2+} and so on. Herein, after the successive addition (200 μM) of interfering substances, there was no reasonable current augmentation caused by adding the species of metal ions, as displayed in Fig. 9(c). This shows that the introduction of unusual species of metal ions does not influence the sensing performance during PE sensing. Subsequently, the continuous addition of an 100 μM excess of biological substances of uric acid (UA), glucose (Glu), ascorbic acid (AA), dopamine (DA), caffeic acid (CA), catechol (CC), and hydroquinone (HQ) was introduced; the interfering compounds of biological substances give corresponding peak responses to their original potential of individual species during the interference study, although no reasonable interaction was observed during PE sensing, as shown in Fig. 9(d). Ultimately, with the consecutive addition of

nitro-aromatics, and pesticides containing species (30 μM) of diphenylamine (DPA), 4-nitrophenol (4-NP), nitrobenzene (NB), diuron (DRN) and methyl parathion (MP) in the presence of PE, we observed less than ±5% error during the interference study, as shown in Fig. 9(e). The calibration plot of I_{pc} $vs.$ interfering compounds of metal ions, biological substance, nitro-aromatics, and pesticide compounds is presented in Fig. 9(f). Thus, this result exhibited that the extensive addition of interfering species will not affect the real-time detection of PE at the front of the La^{3+} doped TiO$_2$ NP decorated f-MWCNT modified GCE electrode. Accordingly, sensing of paraoxon-ethyl (PE) is most effective for the employed potential window of 0.3 to −0.7 V, and in particular sensing onto the La^{3+} doped TiO$_2$ NP decorated f-MWCNT GCE electrode results in an exceptional development in electrochemical sensing performance for PE.

3.2.6. Reproducibility and stability study. The accurate detection of pesticide (PE) is necessary to investigate the reliability of the proposed sensor. Therefore, the reproducibility of the GCE electrode was analyzed with different modified electrodes using La^{3+} doped TiO$_2$ NP decorated f-MWCNTs under similar experimental conditions by adding 50 μM of PE within the potential window of 0.3 to −0.7 V; which are explored by CV techniques (Fig. S4†). The current responses were measured with the relative standard deviation (RSD) of the proposed sensing performance for the individual current response being estimated at 2.39%, revealing that it gives reliable sensing activity with good reproducibility. Moreover, the proposed sensor was analyzed for stability; the reduction peak current responses of PE (50 μM) were recorded at 50 mV s^{-1} by the CV technique. Herein, the stability measurement was carried out three times within 30 days; meanwhile, the fabricated GCE electrode was kept in PBS (pH 7) at $\approx$ 4 °C. The proposed sensor was observed to hold 87.4% of its initial current responses; the suggested sensor gives an outstanding stability response towards PE sensing with an La^{3+} doped TiO$_2$ NP decorated f-MWCNT developed GCE platform.

3.2.7. Real sample analysis. The functional applicability of the recommended sensor was analyzed using soil and water samples. However, because these two samples were collected from New Taipei City, Taiwan, where there is no PE contaminant for practical investigation, a standard addition method was applied. So, a known concentration was introduced into the as-taken working sample by the standard addition method. After collecting the PE contaminated sample, we analyzed the practical response of PE by DPV. The obtained recoveries were in the range of 95.8–100.6% (Table 2), indicating that the modified sensor shows satisfactory results.

4. Conclusion

In summary, the electrochemical sensing performance and mechanisms are reported for a PE sensor with an La^{3+} doped TiO$_2$ NP decorated f-MWCNT modified GCE platform. The recommended sensor abilities were greatly enhanced by the conformal doping of La^{3+} ions into the TiO$_2$ NPs as well as the inclusion of f-MWCNT decorations. The proposed sensor shows an outstanding LOD (0.0019 μM) performance and exceptional

Table 2 Real-time determination of PE in practical samples using the La^{3+} doped TiO$_2$ NP decorated f-MWCNT developed GCE sensor

Sample	Added (μM)	Found (μM)	Recovery (%)
Water sample[a]	0	ND[b]	—
	5	5.03	100.6
	10	9.95	99.5
Soil sample[a]	0	ND[b]	—
	5	4.79	95.8
	10	9.76	97.6

[a] Standard addition method. [b] Not detected.

sensitivity (7.6690 µA µM^{-1} cm^{-2}) on an as-presented catalytic platform of an La^{3+} doped TiO$_2$ NP decorated f-MWCNT modified GCE for a PE sensor. The recommended sensor also showed outstanding performance in terms of reproducibility, stability, and selectivity toward PE detection. We believe that our present approaches to electrochemical PE sensors solve prevailing difficulties and ensure ways to achieve the purpose of low-cost and high-performance pollutant monitoring sensors. Taking advantage of this approach, the good analytical performances of the La^{3+} doped TiO$_2$ NP decorated f-MWCNT modified GCE electrode promotes it as a viable sensor platform for the determination of PE in the environmental sector.

Conflicts of interest

The authors declare that they have no known competing for financial interests or personal relationships that could have appeared to influence the work reported in this paper.

Acknowledgements

References

1 S. Uniyal and R. K. Sharma, *Biosens. Bioelectron.*, 2018, **116**, 37–50.

2 G. G. Pimenta, M. E. de Queiroz, R. P. Victor, L. M. Noronha, A. A. Neves, A. F. d. Oliveira and F. F. Heleno, *J. Braz. Chem. Soc.*, 2017, **28**, 2045–2053.

3 X. Tian, L. Liu, Y. Li, C. Yang, Z. Zhou, Y. Nie and Y. Wang, *Sens. Actuators, B*, 2018, **256**, 135–142.

4 J. E. Chambers and S. F. Oppenheimer, *Toxicol. Sci.*, 2004, **77**, 185–187.

5 S. Marx, A. Zaltsman, I. Turyan and D. Mandler, *Anal. Chem.*, 2004, **76**, 120–126.

6 R. Karthik, J. V. Kumar, S.-M. Chen, T. Kokulnathan, H.-Y. Yang and V. Muthuraj, *ACS Sustainable Chem. Eng.*, 2018, **6**, 8615–8630.

7 J. Wang, W. Chow, D. Leung and J. Chang, *J. Agric. Food Chem.*, 2012, **60**, 12088–12104.

8 Z.-L. Xu, H. Deng, X.-F. Deng, J.-Y. Yang, Y.-M. Jiang, D.-P. Zeng, F. Huang, Y.-D. Shen, H.-T. Lei and H. Wang, *Food Chem.*, 2012, **131**, 1569–1576.

9 E. C. Hopmans, S. Schouten, R. D. Pancost, M. T. van der Meer and J. Sinninghe Damsté, *Rapid Commun. Mass Spectrom.*, 2000, **14**, 585–589.

10 H. Fan, J. Smuts, P. Walsh, D. Harrison and K. Schug, *J. Chromatogr. A*, 2015, **1389**, 120–127.

11 S. Berijani, Y. Assadi, M. Anbia, M.-R. M. Hosseini and E. Aghaee, *J. Chromatogr. A.*, 2006, **1123**, 1–9.

12 X. C. Huang, J. K. Ma, R. X. Feng and S. Wei, *J. Sci. Food Agric.*, 2019, **99**, 6998–7007.

13 A. K. Ravi, P. Navaneeth, P. V. Suneesh, B. G. Nair and T. Babu, *J. Electroanal. Chem.*, 2020, 113841.

14 J. Qiu, S. Zhang and H. Zhao, *Sens. Actuators, B*, 2011, **160**, 875–890.

15 O. A. Zelekew and D.-H. Kuo, *Phys. Chem. Chem. Phys.*, 2016, **18**, 4405–4414.

16 M. M. Mohamed and M. Al-Sharif, *Appl. Catal., B*, 2013, **142**, 432–441.

17 D. Xu, P. Diao, T. Jin, Q. Wu, X. Liu, X. Guo, H. Gong, F. Li, M. Xiang and Y. Ronghai, *ACS Appl. Mater. Interfaces*, 2015, **7**, 16738–16749.

18 M. T. Islam, H. Jing, T. Yang, E. Zubia, A. G. Goos, R. A. Bernal, C. E. Botez, M. Narayan, C. K. Chan and J. Noveron, *J. Environ. Chem. Eng.*, 2018, **6**, 3827–3836.

19 Z.-X. Xu, A.-Q. Wang and Y.-F. Zhu, *Rare Met.*, 2019, **38**, 390–396.

20 Y. Yang, M. Wu, X. Zhu, H. Xu, S. Ma, Y. Zhi, H. Xia, X. Liu, J. Pan and J.-Y. Tang, *Chin. Chem. Lett.*, 2019, **30**, 2065–2088.

21 J. Wang, Y. Zeng, L. Wan, J. Zhao, J. Yang, J. Hu, F. Miao, W. Zhan, R. Chen and F. Liang, *Appl. Surf. Sci.*, 2020, 145301.

22 N. P. Shetti, D. S. Nayak, S. J. Malode and R. Kulkarni, *Sens. Actuators, B*, 2017, **247**, 858–867.

23 H. Chen, M. Shen, R. Chen, K. Dai and T. Peng, *Environ. Technol.*, 2011, **32**, 1515–1522.

24 N. P. Shetti, D. S. Nayak, S. J. Malode and R. Kulkarni, *J. Electrochem. Soc.*, 2017, **164**, B3036–B3042.

25 L. Bazli, M. Siavashi and A. Shiravi, *Compounds*, 2019, **1**, 1–9.

26 G. Rosace, V. Trovato, C. Colleoni, M. Caldara, V. Re, M. Brucale, E. Piperopoulos, E. Mastronardo, C. Milone and G. De Luca, *Sens. Actuators, B*, 2017, **252**, 428–439.

27 J. Liqiang, X. Xiaojun, X. Baifu, W. Baiqi, C. Weimin and F. Honggang, *J. Solid State Chem.*, 2004, **177**, 3375–3382.

28 S. Sadhu and P. Poddar, *RSC Adv.*, 2013, **3**, 10363–10369.

29 W. Guan, F. Ji, Z. Xie, R. Li and N. Mei, *J. Nanomater.*, 2015, **2015**, 4.

30 M. Perez-Cabero, I. Rodrıguez-Ramos and A. Guerrero-Ruız, *J. Catal.*, 2003, **215**, 305–316.

31 U. Kumar and B. Yadav, *J. Taiwan Inst. Chem. Eng.*, 2019, **96**, 652–663.

32 C. Velasco-Santos, A. L. Martínez-Hernández, F. T. Fisher, R. Ruoff and V. Castano, *Chem. Mater.*, 2003, **15**, 4470–4475.

33 G. Trykowski, S. Biniak, L. Stobinski and B. Lesiak, *Acta Phys. Pol., A*, 2010, **118**, 515–518.

34 S. Goyanes, G. Rubiolo, A. Salazar, A. Jimeno, M. Corcuera and I. Mondragon, *Diamond Relat. Mater.*, 2007, **16**, 412–417.

35 F. A. Abuilaiwi, T. Laoui, M. Al-Harthi and M. Atieh, *Arabian J. Sci. Eng.*, 2010, **35**, 37–48.

36 E. S. Babu, B. J. Rani, G. Ravi, R. Yuvakkumar, R. K. Guduru, V. Ganesh and S. Kim, *Mater. Lett.*, 2018, **220**, 209–212.

37 A. M. Ruiz, A. Cornet and J. R. Morante, *Sens. Actuators, B*, 2005, **111**, 7–12.

38 A. M. Ruiz, A. Cornet and J. Morante, *Sens. Actuators, B*, 2005, **111**, 7–12.

39 R. Shwetharani, A. Poojashree, G. R. Balakrishna and M. Jyothi, *New J. Chem.*, 2018, **42**, 1067–1077.

40 H. Ago, T. Kugler, F. Cacialli, W. R. Salaneck, M. S. Shaffer, A. H. Windle and R. H. Friend, *J. Phys. Chem. B*, 1999, **103**, 8116–8121.

41 E. Mickelson, C. Huffman, A. Rinzler, R. Smalley, R. Hauge and J. Margrave, *Chem. Phys. Lett.*, 1998, **296**, 188–194.

42 Z. Rastian, A. A. Khodadadi, F. Vahabzadeh, C. Bortolini, M. Dong, Y. Mortazavi, A. Mogharei, M. V. Naseh and Z. Guo, *Biochem. Eng. J.*, 2014, **90**, 16–26.

43 B. Ding, C. Han, L. Zheng, J. Zhang, R. Wang and Z. Tang, *Sci. Rep.*, 2015, **5**, 9443.

44 Y. Zhang, W. Hong, Y. Zhang, W. Xu, Z. Shi, X. Li, H. Hou and X. Ji, *Electrochim. Acta*, 2018, **283**, 1514–1524.

45 P. T. Kissinger and W. R. Heineman, *J. Chem. Educ.*, 1983, **60**, 702.

46 Y. Li, L. Zou, G. Song, K. Li and B. Ye, *J. Electroanal. Chem.*, 2013, **709**, 1–9.

47 N. Erk, *Anal. Bioanal. Chem.*, 2004, **378**, 1351–1356.

48 Y. V. M. Reddy, S. Bathinapatla, T. Łuczak, M. Osińska, H. Maseed, P. Ragavendra, L. S. Sarma, V. Srikanth and G. Madhavi, *Biosens. Bioelectron.*, 2018, **42**, 3137–3146.

49 V. Renganathan, R. Balaji, S.-M. Chen and T. Kokulnathan, *Sens. Actuators, B*, 2020, **307**, 127586.

50 J. Wang, L. Chen, A. Mulchandani, P. Mulchandani and W. Chen, *Electroanalysis*, 1999, **11**, 866–869.

51 T. Laothanachareon, V. Champreda, P. Sritongkham, M. Somasundrum and W. Surareungchai, *World J. Microbiol. Biotechnol.*, 2008, **24**, 3049.

52 R. P. Deo, J. Wang, I. Block, A. Mulchandani, K. A. Joshi, M. Trojanowicz, F. Scholz, W. Chen and Y. Lin, *Anal. Chim. Acta*, 2005, **530**, 185–189.

53 H. Bagheri, A. Afkhami, H. Khoshsafar, A. Hajian and A. Shahriyari, *Biosens. Bioelectron.*, 2017, **89**, 829–836.

54 A. Aghaie, A. Khanmohammadi, A. Hajian, U. Schmid and H. Bagheri, *Food Anal. Methods*, 2019, **12**, 1545–1555.